ADVANCED OPTICAL MATERIALS
www.advopticalmat.de

Influence of Hot Carrier Cooling and Band-Filling Effect on Linewidth of Perovskite Microlasers

Peipei Ma, Jinhai Si, Lihe Yan, Jiayi Wu, Jin Xu, and Xun Hou*

In semiconductor-based microlasers, the generated excited carriers can affect both the optical absorption coefficient and refractive index, influencing the lasing behavior and device performance. In this study, the lasing behavior of individual $MAPbBr_3$ microrods pumped by femtosecond laser pulses is investigated using an ultrafast optical Kerr gating technique. By analyzing the spectral and temporal evolution of the lasing behavior, it is found that the band-filling (BF) effect can cause a significant change in the refractive index of the material, which results in an unfavorable red-shift and broadening of the resonant modes, deteriorating the laser linewidth and quality factor. The hot carrier cooling process can provide a buffer for alteration of the energy level occupation state, resulting in a small transient refractive index change and slight red-shift. These results offer insights into the lasing behavior driven by photogenerated carrier dynamics and provide an optimization strategy for semiconductor-based microlasers.

1. Introduction

Semiconductor-based micro/nanolasers are desirable for on-chip optical interconnections due to their small scale, high integration, low power consumption, and anti-electromagnetic interference.[1] Self-assembly micro/nanostructures, including micro/nanosheets, micro/nanorods, microspheres, and thin films, have been demonstrated as simple and efficient approaches for micro/nanolasers.[2] Self-assembly micro/nanolasers with well-defined lasing actions have been developed based on diverse semiconductor gain media including ZnO, GaN, InP, and their multi-quantum well derivatives.[3] Metal halide perovskites have recently become competitive gain medium candidates owing to their high absorption coefficient ($>10^4$ cm^{-1}), tunable direct bandgap across the visible spectrum, and high fluorescence yield.[4] A high gain coefficient,[5] ultra-high quality factor,[6] low threshold,[7] and continuous-wave lasing[8] have been realized via material and structural engineering in previous research.

Halide perovskite-based micro/nanolasers are usually operated using pulsed laser pumping. Many studies have been conducted to enhance device performance, including the pulse duration, linewidth, and quality factor. The performance is closely related to the dynamics of the photogenerated carriers during operation, including carrier generation, hot carrier relaxation, carrier recombination, and other processes.[9] Thus, understanding the photogenerated carrier dynamics in individual devices is crucial for optimizing the performance of micro/nanolasers. As these processes occur on the sub-picosecond to nanosecond timescale, it is challenging to directly measure the intrinsic relationship between the photogenerated carrier dynamics and device parameters.

In this study, we investigated the lasing dynamics of individual $MAPbBr_3$ microrods using a femtosecond time-resolved optical Kerr gating technique. Through analysis of the spectral and temporal evolution of lasing, the photogenerated carrier dynamics and their effects on the lasing properties were explored. The red-shifts and broadening of the full width at half-maximum (FWHM) of the lasing resonant modes in the time domain induced by the BF effect deteriorated the lasing linewidth and quality. The hot carrier cooling process provided a buffer for the giant BF effect and relieved the red-shift. We hope that our observations of carrier dynamics related to lasing properties will provide an optimization strategy for perovskite-based microlasers.

2. Results and Discussion

$MAPbBr_3$ microrods were synthesized using liquid self-assembly combined with an anti-solvent diffusion growth method, as described in the Experimental Section. To evaluate the optical properties of the $MAPbBr_3$ microrods, steady-state absorption and photoluminescence (PL) spectra were measured using a home-built micro-absorption and micro-PL setup (Sections S1 and S2, Supporting Information). The absorption spectrum in **Figure 1a** displays a sharp band-edge cutoff ≈520 nm, consistent with previous studies.[10] The steady-state PL spectrum showed an emission centered at 538 nm with an FWHM of 27 nm. The sharp

P. Ma, J. Si, L. Yan, J. Wu, J. Xu, X. Hou
Key Laboratory for Physical Electronics and Devices of the Ministry of Education & Shaanxi Key Lab of Photonic Technique for Information
School of Electronics Science & Engineering
Faculty of Electronic and Information Engineering
Xi'an Jiaotong University
Xi'an 710049, China
E-mail: jinhaisi@mail.xjtu.edu.cn

J. Xu
School of Electronics Engineering and Computer Science
Peking University
Beijing 100871, China

The ORCID identification number(s) for the author(s) of this article can be found under https://doi.org/10.1002/adom.202400189

DOI: 10.1002/adom.202400189

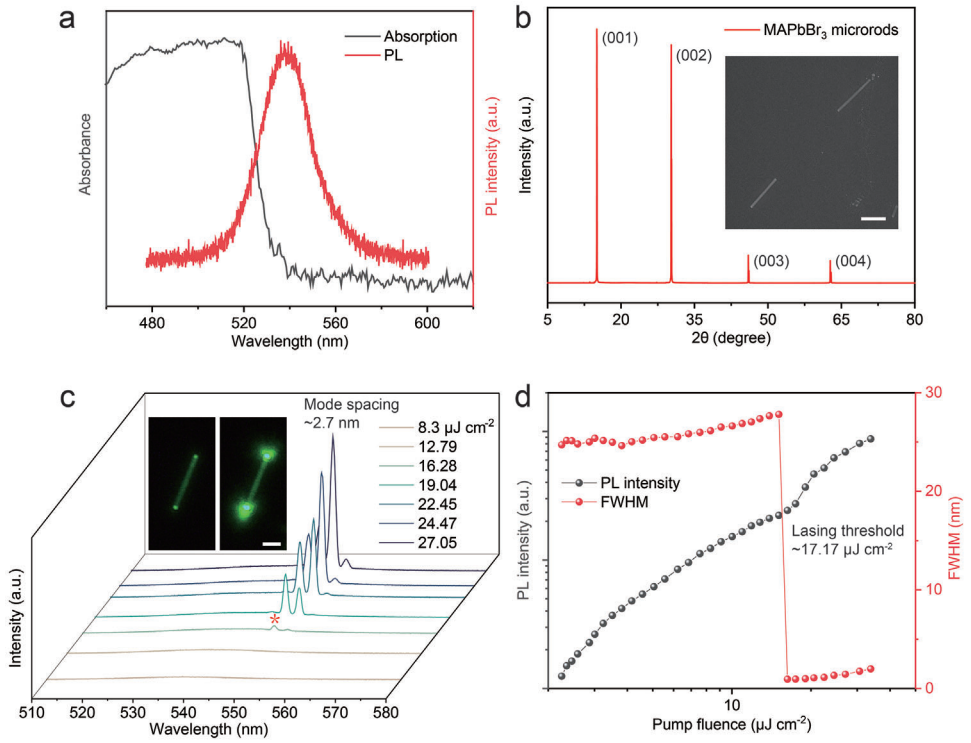

Figure 1. a) Steady-state absorption and PL spectra of $MAPbBr_3$ microrods. b) XRD pattern of $MAPbBr_3$ microrods. The inset shows a SEM image of $MAPbBr_3$ microrods. Scale bar, 5 μm. c) Pump fluence-dependent emission spectra of individual $MAPbBr_3$ microrod. The insets are fluorescence images below (left panel) and above (right panel) the lasing threshold of the $MAPbBr_3$ microrod. Scale bar, 5 μm. d) Evolution of integrated emission intensity and FWHM as a function of pump fluence. The fitting FWHM values above the threshold were extracted from the resonant mode with an asterisk marked in Figure 1c.

absorption band-edge and narrow FWHM indicate high crystallinity and few defect states in the sample. Morphological information was obtained using scanning electron microscopy (SEM) (inset in Figure 1b). The longitudinal length of the $MAPbBr_3$ microrods ranged from a few microns to tens of microns; their lateral dimensions were hundreds of nanometers. To demonstrate the single-crystal nature of $MAPbBr_3$ microrods, X-ray diffraction (XRD) measurements were performed, as shown in Figure 1b. Four main peaks appeared at 15.04°, 30.25°, 45.99°, and 62.73°, indexed to the (001), (002), (003), and (004) crystal planes of the $MAPbBr_3$ cubic phase. The ω-rocking curve of the (001) diffraction peak showed a narrow FWHM of ≈199 arcsec, indicating good crystallinity (Section S3, Supporting Information).

The representative pump fluence-dependent emission spectra plotted in Figure 1c were obtained using a micro-PL setup. By adjusting the distance between the sample and the focusing objective lens, the microrod was uniformly excited by 400 nm femtosecond laser pulses. At lower pump fluences ($P \leq 12.79$ μJ cm^{-2}), the emission peaks were located at 538 nm with a broad FWHM of ≈26.5 nm, corresponding to the spontaneous emission of $MAPbBr_3$. As the pump fluence increased, several sharp peaks appeared at the long-wavelength shoulder of the broad PL peak, corresponding to the lasing modes generated in the Fabry–Perot (F–P) cavity formed by the end faces of the microrod. These resonant modes with narrow FWHM showed high intensity, far exceeding the PL peaks; the axial mode spacing was estimated to be ≈2.7 nm. The light-in-light-out data as a function of the pump fluence, shown in Figure 1d, gave a lasing threshold of ≈17.17 μJ cm^{-2}. The sudden drop in the FWHM with increasing pump fluence confirms lasing generation. The fluorescence image of the microrod below the lasing threshold shows a low-intensity but spatially uniform emission (left inset in Figure 3c). When the pump fluence increased above the threshold, two bright light spots were observed on the two end facets along the axis of the microrod due to the strong waveguiding effect of the microrod (right inset in Figure 1c). The experimental mode spacing for microrods of different lengths is linearly related to the reciprocal of the length, which confirms the F–P longitudinal cavity modes (Section S4, Supporting Information).

Although the lasing properties of the microrods can be obtained, the emission spectra are integrated results for the entire emission time, and the temporal and spectral evolutions of the emission and their influence on the lasing properties are not reflected. Ultrafast spectroscopy technologies such as temporal-resolved emission spectroscopy and transient absorption (TA) spectroscopy are effective approaches to recognize the light–matter interactions in materials, including excited carrier and photon dynamics and photo- and electro-luminescence mechanisms.[11] In this study, we used a microscopic optical Kerr gating technique to study the lasing dynamics of individual $MAPbBr_3$ microrods. The homebuilt setup provided a subpicosecond temporal resolution and a sub-micron spatial resolution (Section S2, Supporting Information). By adjusting the delay time of the optical Kerr gate and the emission pulse, the

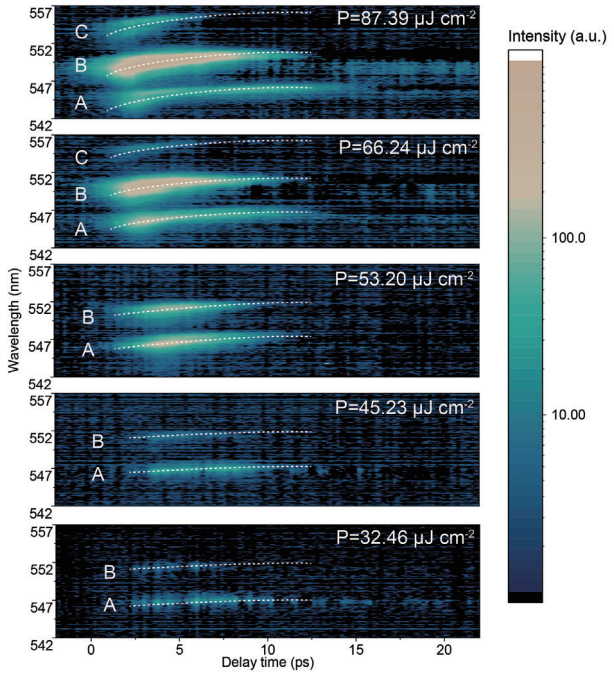

Figure 2. Spectral and temporal resolved emission behavior of $MAPbBr_3$ microrod as a function of pump fluence.

temporal-resolved emission spectra of individual $MAPbBr_3$ microrod were obtained. The corresponding delay time of the emission emergence was defined as the zero-delay time. The temporal and spectral evolutions of the emission with different pump fluences above the lasing threshold are presented in **Figure 2**. The variation trend can be summarized as follows: 1) With increasing pump fluence, a new resonant mode (as shown by mode C with pump fluences of 66.24 and 87.39 μJ cm^{-2}) appears on the long-wavelength sides of initial modes A and B; 2) With increasing pump fluence, the build-up time (defined as the time interval between the emission peak and zero-delay time) is gradually shortened; 3) Each mode shifts to the lower-energy side with increasing delay time. The instantaneous frequency shifts in the lasing dynamics result in the broadening of the linewidth.[9a,11c]

The appearance of the new mode is due to the red-shift of the gain spectra induced by the bandgap renormalization (BGR) effect. When the pump fluence increases, the excited carrier density increases; a many-body effect and screening of the electron-hole Coulomb interaction can occur at a high excited carrier density (>10^{17} cm^{-3}). These effects cause a reduction in the bandgap and a red-shift in the gain profile (BGR effect).[12] Here, the initial excited carrier density under fs-pulsed laser excitation was evaluated as 10^{18} cm^{-3} orders of magnitude (Section S5, Supporting Information), which can induce a strong BGR effect.

For a deeper understanding of the lasing dynamics of the microrod, we plotted the emission intensity evolution of mode A as a function of the delay time and pump fluence, as shown in **Figure 3a**. The build-up time of mode A was shortened by ≈2 ps as the pump fluence increased from 32.46 to 87.39 μJ cm^{-2} due to a greater stimulated transition probability at a higher pump fluence.[13] The weakening of emission intensity as the pump fluence increased from 53.20 to 87.39 μJ cm^{-2} was a result of the BGR effect and a red-shift of the gain profile, which weakened the gain of mode A. The decay process of this stimulated emission (SE) can be fitted by a mono-exponential function; the fitting lifetime (τ) is presented in the table in Figure 3a. It is observed that the lifetime prolonged from 2.34 to 3.73 ps when the pump fluence increased from 53.20 to 87.39 μJ cm^{-2}. Considering hot carrier lifetimes of up to tens of picoseconds with increasing pump fluence (**Figure 4d**), the prolonged SE decay process was attributed to the involvement of the cooling hot carriers.

Typical emission spectra of mode A at different delay times are shown in Figure 3b. An obvious red-shift of the lasing mode is observed with increasing delay time; the red-shift can reach ≈1.25 nm when the delay time increases from 0.6 to 10.6 ps. The FWHM of the transient emission spectrum also varies; for example, the FWHM at 2.6 ps delay time is narrower than that at 0.6 ps delay time. To investigate the spectral evolution of lasing, we plotted the dynamics of the central wavelength (λ_c) and FWHM of resonant mode A in Figure 3c. It is observed that λ_c evolves with a nonlinear trend that can be summarized in two stages: 1) λ_c remained almost constant from the initial delay time to ≈2.4 ps; 2) λ_c red-shifted exponentially from ≈2.4 ps delay time to the end. Moreover, the FWHM of the lasing mode gradually narrowed and remained almost constant after ≈5 ps delay time.

The red-shift of the resonant mode originates from a carrier-induced change in the material refractive index. Two factors can affect the refractive index in the excited state: the change in the occupied state of the energy band and the change in the bandgap (for example, BGR effect).[14] When the sample is excited by a laser pulse, the filling of electron states in the conduction band and hole states in the valence band causes bleaching of optical interband transitions, known as the band-filling (BF) effect. Both the BF and BGR effects can affect the absorption of the material. The former can result in a decrease in the absorption coefficient near the bandgap; the latter can lead to an increase.[14] The refractive index can be obtained from the absorption coefficient using the Kramers–Kronig relationship. A simulation of the refractive index change induced by the BF and BGR effects as a function of carrier density is presented in Section S6 (Supporting Information), which shows an increase in the refractive index with a decrease in the excited carrier density.

In the first stage, the SE and hot carrier cooling processes occur simultaneously. The SE process consumes the excited carriers and leaves the filling energy state unoccupied. Relaxation of hot carriers to the ground state with lifetimes of up to tens of picoseconds offsets these releases.[13] Thus, the refractive index of the material remains almost constant despite a decrease in the overall carrier density. Moreover, the contribution of the hot carriers is more pronounced at higher pump fluence levels, as shown in Section S7 (Supporting Information), coinciding with the increasing lifetime of the hot carriers. Subsequently, with the recombination of abundant excited carriers and insufficient relaxation of hot carriers, the energy level occupancy states are released and λ_c red-shifts exponentially due to the carrier density decreasing and induced transient refractive index increasing.

Moreover, the emission FWHM at room temperature broadens due to electron–phonon coupling, which is an approach to the hot carrier cooling process. At higher hot carrier temperatures, strong electron–phonon coupling broadens the emission line.[15] Thus, the FWHM of mode A tends to narrow with in-

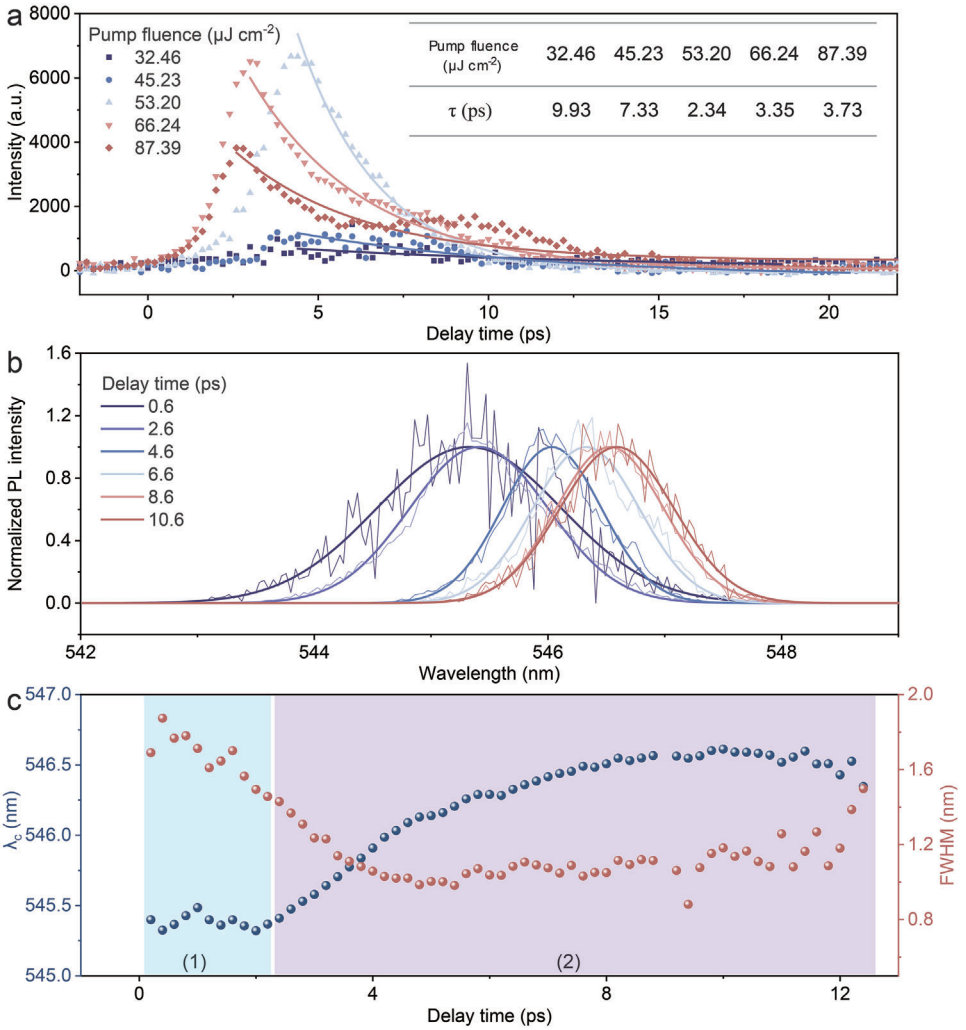

Figure 3. a) Emission intensity dynamics of mode A as a function of pump fluence. The inserted table shows the fitting lifetime of the SE delay process at different pump fluences. b) Typical emission spectra of mode A with different delay times with pump fluence of 66.24 μJ cm^{-2}. c) Dynamics of the central wavelength (λ_c) and FWHM of mode A with pump fluence of 66.24 μJ cm^{-2}.

creasing delay time owing to a weakened BF effect and electron–phonon coupling induced by the decreased excited carrier density. Following exhaustion of the hot carriers, the FWHM remained almost constant. The giant BF effect and strong electron–phonon coupling resulted in high carrier recombination rates and a dramatic red-shift, while the FWHM of the resonant modes broadened, which had a significant impact on the linewidth and quality of the laser modes.

Femtosecond TA measurements were also performed to further verify the carrier behaviors involved in the SE process, mainly the hot carrier cooling process and the BF effect. The TA spectra of the $MAPbBr_3$ microcrystal in Figure 4a show negative peaks centered at ≈529 nm, corresponding to band-edge photobleaching (PB) signals. The positions and shapes of the PB peaks reflect the bandgap evolution and hot carrier dynamics because PB signals monitor the occupancy of the states at the band-edge.[16] As shown in Figure 4b, the PB peak shows a persistent red-shift with increasing delay time at lower pump fluences (P = 23.66 and 29.39 μJ cm^{-2}), and a blue-shift followed by a red-shift at higher pump fluences (P = 37.64, 57.36, and 82.45 μJ cm^{-2}). The red-shift of up to tens of picoseconds is regarded as bandgap shrinkage induced by the decreasing carrier density and weakened BF effect.[16a] The blue-shift of the PB peak with increasing pump fluence and carrier density, as shown in Figure 4c, indicates the dominant role of the BF effect on the band-edge bleach signal compared to the BGR effect. The hot carrier temperature and cooling dynamics were achieved by fitting the high-energy tail of the PB peaks with a Maxwell–Boltzmann function, as shown in Figure 4d.[11b] The effects of the hot carrier cooling process on the band-edge states are reflected in the prolonged SE decay lifetime and the initial blue-shift of the PB signals as the pump fluence increases, as the cut-off time of the blue-shift matches the lifetime of the hot carriers.

Figure 5 shows a schematic representation of the photogenerated carrier dynamics and their effects on the energy-band structure during the SE process in $MAPbBr_3$ microlasers, which helps in understanding the spectral and temporal evolution of lasing emission. First, after femtosecond pulsed laser excitation and a

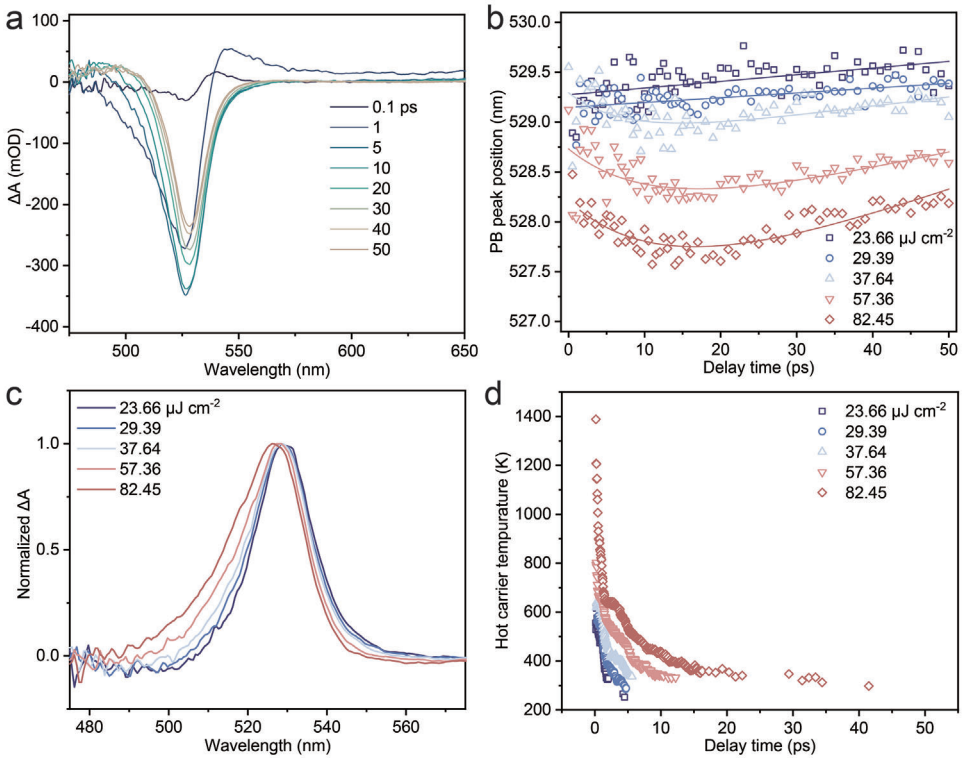

Figure 4. a) TA spectra at different delay times for $MAPbBr_3$ single crystal with a pump fluence of 82.45 μJ cm^{-2}. b) Dynamic evolution of PB peak position at different pump fluences. c) Normalized TA spectra at different pump fluences with a delay time of 2 ps. d) Fitting hot carrier temperature as a function of delay time at different pump fluences.

quick carrier thermalization process, the photogenerated carriers fill the states at the conduction and valence band-edges. Following the principle of Pauli exclusion and many-body interaction, the occupation of band-edge states forces a higher-energy optical transition (BF effect), and the screening of the electron-hole Coulomb interaction reduces the optical bandgap (BGR effect). Usually, the weakening of BF and BGR effects with time and a decrease in carrier density increases the group refractive index near the resonant photon energy. However, when the hot carrier cooling process is sufficiently long to affect the SE process, relaxation of the hot carrier offsets the release of the energy state and leaves the occupation state unchanged, resulting in few changes in the refractive index and mode shift. Meanwhile, strong electron–phonon coupling broadens the emission

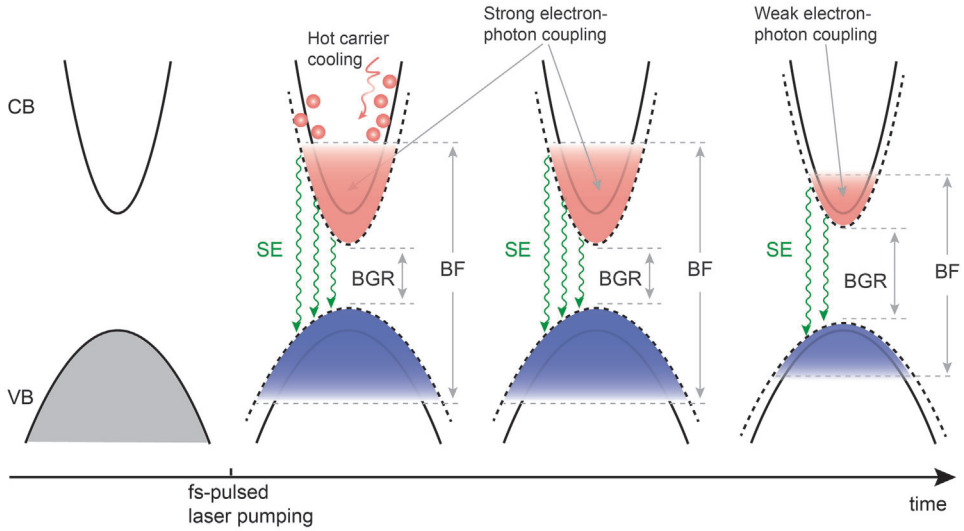

Figure 5. Diagram of dominant carrier behaviors and induced effects with time after femtosecond pulsed laser excitation.

linewidth. Due to the large emission and recombination of excited carriers, changes in the refractive index and a red-shift induced by the BF effect occur, and the emission linewidth gradually narrows. Finally, the BF effect becomes insignificant, and weak electron–phonon coupling results in a constant emission linewidth.

3. Conclusion

We used femtosecond temporal-resolved emission spectra to investigate the carrier and lasing dynamics in $MAPbBr_3$ microrods. Red-shifts of the resonant modes and broadening of the lasing mode linewidth in the time domain were detected, attributed to the giant BF effect. The hot carrier cooling process relieved the red-shift by providing a buffer pathway for the giant BF effect. We expect that these findings on carrier-behavior-dependent lasing dynamics will help researchers in designing high-quality perovskite microlasers.

4. Experimental Section

Synthesis of $MAPbBr_3$ Microrods: $MAPbBr_3$ microrods were obtained through liquid self-assembly combined with an anti-solvent diffusion growth method. First, methylammonium bromide (CH_3NH_3Br, 99.5%, Xi'an Baolaite) and lead (II) bromide ($PbBr_2$, 99%, Meryer) were dissolved in N,N-dimethylformamide (DMF, >99.9%, Aladdin) at a concentration of 0.5 mmol mL^{-1}. The mixture was stirred at 40 °C for 3 h to achieve a transparent precursor solution. Next, 1 µL of precursor solution was dispersed on a quartz substrate, covered with another quartz substrate, and transferred into a sealed container at 60 °C for 12 h. A beaker filled with 20 mL of toluene (≥99.5%, Sinopharm) was also placed in the sealed container, providing an anti-solvent atmosphere.

Femtosecond Temporal-Resolved Emission Spectra: Transient emission spectra were measured using a homebuilt optical Kerr gated fluorescence microscope. A femtosecond laser pulse train (central wavelength: 800 nm, pulse width: ≈50 fs, repetition rate: 1 kHz) from a Ti:sapphire regenerative amplifier was divided into two beams. One part passed through a mechanical delay stage and induced birefringence in the nonlinear Kerr medium, which acted as a gating beam. The other part was sent to a BBO crystal to generate a 400 nm excitation beam and focused on the samples using an objective (40×, NA = 0.75) to excite the photoluminescence emission. After passing through the linear polarizer, the photoluminescence was focused onto an optical Kerr medium with a gating pulse. After passing through the Kerr medium, the polarization of the photoluminescence signals was changed; parts of the beam were transmitted through the analyzer. Temporal-resolved photoluminescence spectra were recorded using a spectrometer by adjusting the delay time between the gating and photoluminescence pulses. The measurements were performed in ambient conditions. The spatial and temporal resolutions of the microscopic optical Kerr gating measurements were estimated to be greater than 0.8 µm and 400 fs, respectively.

Supporting Information

Supporting Information is available from the Wiley Online Library or from the author.

Acknowledgements

This work was supported by the National Natural Science Foundation of China (Grant No. 62027822) and the National R&D Program of China (Grant No. 2019YFA0706402). F. Lin from Shaanxi Key Lab of Photonic Technique for Information was thanked for the measurement of ω-rocking curve.

Conflict of Interest

The authors declare no conflict of interest.

Data Availability Statement

The data that support the findings of this study are available from the corresponding author upon reasonable request.

Keywords

band-filling effect, carrier dynamics, lasing dynamics, perovskite microlasers, ultrafast spectroscopy

Received: January 21, 2024
Revised: March 8, 2024
Published online:

[1] R. M. Ma, R. F. Oulton, *Nat. Nanotechnol.* **2019**, *14*, 12.
[2] a) L. Liu, H. Yao, H. Li, Z. Wang, Y. Shi, *Flatchem.* **2018**, *10*, 22; b) W. Zhang, J. Yao, Y. S. Zhao, *Acc. Chem. Res.* **2016**, *49*, 1691.
[3] a) K. Tang, M. Jiang, P. Wan, C. Kan, *Opt. Express.* **2021**, *29*, 983; b) F. Tabataba-Vakili, L. Doyennette, C. Brimont, T. Guillet, S. Rennesson, E. Frayssinet, B. Damilano, J. Y. Duboz, F. Semond, I. Roland, M. El Kurdi, X. Checoury, S. Sauvage, B. Gayral, P. Boucaud, *ACS Photonics.* **2018**, *5*, 3643; c) Y. Zhang, H. Song, L. Wang, J. Yu, B. Wang, Y. Hu, S.-Q. Zang, B. Yang, S. Lu, *Angew. Chem., Int. Ed.* **2021**, *60*, 25514; d) X. Zhuang, Y. Ouyang, X. Wang, A. Pan, *Adv. Opt. Mater.* **2019**, *7*, 1900071.
[4] a) Y. Fu, H. Zhu, J. Chen, M. P. Hautzinger, X.-Y. Zhu, S. Jin, *Nat. Rev. Mater.* **2019**, *4*, 169; b) S. De Wolf, J. Holovsky, S. J. Moon, P. Loper, B. Niesen, M. Ledinsky, F. J. Haug, J. H. Yum, C. Ballif, *J. Phys. Chem. Lett.* **2014**, *5*, 1035; c) I. L. Braly, D. W. de Quilettes, L. M. Pazos-Outón, S. Burke, M. E. Ziffer, D. S. Ginger, H. W. Hillhouse, *Nat. Photonics.* **2018**, *12*, 355; d) A. Dey, J. Ye, A. De, E. Debroye, S. K. Ha, E. Bladt, A. S. Kshirsagar, Z. Wang, J. Yin, Y. Wang, L. N. Quan, F. Yan, M. Gao, X. Li, J. Shamsi, T. Debnath, M. Cao, M. A. Scheel, S. Kumar, J. A. Steele, M. Gerhard, L. Chouhan, K. Xu, X. G. Wu, Y. Li, Y. Zhang, A. Dutta, C. Han, I. Vincon, A. L. Rogach, et al., *ACS Nano.* **2021**, *15*, 10775.
[5] B. R. Sutherland, S. Hoogland, M. M. Adachi, P. Kanjanaboos, C. T. Wong, J. J. McDowell, J. Xu, O. Voznyy, Z. Ning, A. J. Houtepen, E. H. Sargent, *Adv. Mater.* **2015**, *27*, 53.
[6] a) C. S. Wu, S. C. Wu, B. T. Yang, Z. Y. Wu, Y. H. Chou, P. Chen, H. C. Hsu, *ACS Appl. Mater. Interfaces.* **2021**, *13*, 13556; b) V. S. Chirvony, I. Suárez, J. Sanchez-Diaz, R. S. Sánchez, J. Rodríguez-Romero, I. Mora-Seró, J. P. Martínez-Pastor, *Adv. Mater.* **2023**, *35*, 2208293.
[7] H. Zhu, Y. Fu, F. Meng, X. Wu, Z. Gong, Q. Ding, M. V. Gustafsson, M. T. Trinh, S. Jin, X.-Y. Zhu, *Nat. Mater.* **2015**, *14*, 636.
[8] D. H. Nguyen, J. Y. Sun, C. Y. Lo, J. M. Liu, W. S. Tsai, M. H. Li, S. J. Yang, C. C. Lin, S. D. Tzeng, Y. R. Ma, M. Y. Lin, C. C. Lai, *Adv. Mater.* **2021**, *33*, 2006819.
[9] a) J. Wang, G. Liu, W. Liu, Y. Chen, X. Cheng, H. Yang, Y. Gao, L. Xiao, S. Wang, Q. Gong, *J. Phys. Chem. C.* **2022**, *126*, 14922; b) L. Lei, D. Seyitliyev, S. Stuard, J. Mendes, Q. Dong, X. Y. Fu, Y. A. Chen, S. L. He, X. P. Yi, L. P. Zhu, C. H. Chang, H. Ade, K. Gundogdu, F. So, *Adv. Mater.* **2020**, *32*; c) Q. L. Zhang, H. W. Liu, P. F. Guo, D. Li, P. Fan, W. H. Zheng, X. L. Zhu, Y. Jiang, H. Zhou, W. Hu, X. J. Zhuang, H. J. Liu, X. F. Duan, A. L. Pan, *Nano Energy.* **2017**, *32*, 28; d) X. Zeng, Z. Z. Liu, H. J. Du, Z. J. Wang, M. H. Li, M. Y. Pi, J. J. Tan, D. K. Zhang, J. Yang, J. Du, *Adv. Opt. Mater.* **2022**, *10*, 2201328; e) D. Yamashita, Y. Takahashi, J. Kurihara, T. Asano, S. Noda, *Phys. Rev. Appl.* **2018**, *10*,

024039; f) C. Wang, L. Yan, J. Si, T. Huo, X. Hou, *J. Alloys Compd.* **2023**, *946*, 169272; g) J. Qin, X.-K. Liu, C. Yin, F. Gao, *Trends Chem.* **2021**, *3*, 34.

[10] S. Yan, K. Wang, G. Xing, J. Xu, S. Su, Z. Tang, S. Wang, K. W. Ng, *ACS Appl. Mater. Interfaces.* **2021**, *13*, 38458.

[11] a) W. Liu, H. Yu, Y. Li, A. Hu, J. Wang, G. Lu, X. Li, H. Yang, L. Dai, S. Wang, Q. Gong, *Nano Lett.* **2021**, *21*, 2932; b) Y. Yang, D. P. Ostrowski, R. M. France, K. Zhu, J. van de Lagemaat, J. M. Luther, M. C. Beard, *Nat. Photonics.* **2016**, *10*, 53; c) J. Tian, G. Weng, Y. Liu, S. Chen, F. Cao, C. Zhao, X. Hu, X. Luo, J. Chu, H. Akiyama, S. Chen, *Commun. Phys.* **2022**, *5*, 160.

[12] a) J. Qin, Y. Tang, J. Zhang, T. Shen, M. Karlsson, T. Zhang, W. Cai, L. Shi, W.-X. Ni, F. Gao, *Mater. Horiz.* **2023**, *10*, 1446; b) A. P. Schlaus, M. S. Spencer, K. Miyata, F. Liu, X. Wang, I. Datta, M. Lipson, A. Pan, X. Y. Zhu, *Nat. Commun.* **2019**, *10*, 265; c) G. Weng, J. Tian, S. Chen, J. Yan, H. Zhang, Y. Liu, C. Zhao, X. Hu, X. Luo, J. Tao, S. Chen, Z. Zhu, J. Chu, H. Akiyama, *ACS Photonics.* **2021**, *8*, 787.

[13] P. Ma, L. Yan, J. Si, T. Huo, Z. Huang, W. Tan, J. Xu, X. Hou, *Laser Photonics Rev.* **2023**, *17*, 2300533.

[14] B. R. Bennett, R. A. Soref, J. A. Del Alamo, *IEEE J. Quantum Electron.* **1990**, *26*, 113.

[15] a) C. Wehrenfennig, M. Z. Liu, H. J. Snaith, M. B. Johnston, L. M. Herz, *J. Phys. Chem. Lett.* **2014**, *5*, 1300; b) A. D. Wright, C. Verdi, R. L. Milot, G. E. Eperon, M. A. Pérez-Osorio, H. J. Snaith, F. Giustino, M. B. Johnston, L. M. Herz, *Nat. Commun.* **2016**, *7*, 11755.

[16] a) J. S. Manser, P. V. Kamat, *Nat. Photonics.* **2014**, *8*, 737; b) M. Li, J. Fu, Q. Xu, T. C. Sum, *Adv. Mater.* **2019**, *31*, 1802486; c) T. Huo, L. Yan, J. Si, P. Ma, X. Hou, *J. Mater. Chem. C.* **2023**, *11*, 3736.